Research Square

Preprints are preliminary reports that have not undergone peer review.
They should not be considered conclusive, used to inform clinical practice,
or referenced by the media as validated information.

# Unsupervised Satellite Image Change Detection Using Quantum-Inspired Mapping and Weighted Hybrid Neighborhood MRFs

**Saman Ghafari**[1]

samanghafari252@gmail.com

Amirkabir University of Technology https://orcid.org/0009-0005-0988-8346

**Shaho Piroti**

Department of Remote Sensing and GIS, Kharazmi University, Tehran, Iran https://orcid.org/0009-0009-3502-8576

**Parviz Zeaieanfirouzabadi**

Department of Remote Sensing and GIS, Kharazmi University, Tehran, Iran https://orcid.org/0000-0002-6510-3786

**Method Article**

**Keywords:** satellite images, Change Detection, Markov Random Field, Quantum-Inspired Computing, Simulated Annealing

**Posted Date:** August 31st, 2026

**DOI:** https://doi.org/10.21203/rs.3.rs-10845063/v1

**License:** This work is licensed under a Creative Commons Attribution 4.0 International License.
Read Full License

**Additional Declarations:** The authors declare no competing interests.

# Unsupervised Satellite Image Change Detection Using Quantum-Inspired Mapping and Weighted Hybrid Neighborhood MRFs

Saman Ghafari[1]*, Shaho Piroti[2], Parviz Zeaieanfirouzabadi[2]

[1] Department of Physics and Energy Engineering, Tehran Polytechnic, Tehran, Iran

[2] Department of Remote Sensing and GIS, Kharazmi University, Tehran, Iran

* Corresponding author

E-mail: samanghafari252@gmail.com

**ORCID:**
Saman Ghafari: https://orcid.org/0009-0005-0988-8346
Shaho Piroti: https://orcid.org/0009-0009-3502-8576
Parviz Zeaieanfirouzabadi: https://orcid.org/0000-0002-6510-3786

## Abstract

Unsupervised change detection (CD) in bi-temporal remote sensing imagery is an important task in Earth observation, but conventional approaches based on spatially invariant regularization may be sensitive to radiometric noise and may suffer from excessive boundary smoothing in heterogeneous scenes. In this study, we propose a context-aware change detection framework that reformulates a patch-decomposed Markov Random Field (MRF) as a Quadratic Unconstrained Binary Optimization (QUBO) problem, providing a formulation compatible with quantum annealing architectures. A context-aware beta formulation is introduced to determine the spatial smoothness strength from localized patch statistics rather than using a globally fixed regularization parameter. In addition, the conventional 4-connected neighborhood is extended to a weighted 8-connected topology, in which diagonal interactions are scaled by the inverse Euclidean distance factor to account for their longer spatial separation. Although the resulting QUBO formulation is designed to support quantum annealing, the experiments in this study are performed using a classical Simulated Annealing (SA) solver. The proposed framework is evaluated on the Onera Satellite Change Detection (OSCD) benchmark dataset without supervised training or external labeled data. Across the evaluated scenes, the proposed method achieves an average F1-score of 0.3483, an Overall Accuracy of 96.15%, and a Cohen's Kappa of 0.3323. The results demonstrate that combining context-aware spatial regularization with distance-weighted neighborhood interactions provides a training-free MRF-QUBO framework for unsupervised change detection while retaining compatibility with future quantum annealing implementations.

**Keywords:** satellite images, Change Detection, Markov Random Field, Quantum-Inspired Computing, Simulated Annealing.

## 1. Introduction

Change detection (CD) in remote sensing is a fundamental task in Earth observation that aims to identify and characterize land-cover or land-use transitions between observations acquired at different times over the same geographic region (Chen and Bruzzone 2022; Cheng et al. 2024). The increasing availability of high-resolution and multi-temporal satellite imagery has expanded the applications of CD to urban expansion monitoring (Liu et al. 2021), agricultural assessment (Misra et al. 2026), forest and environmental monitoring (Bruzzone and Prieto 2000), and disaster damage assessment (Brunner et al. 2010; Buch et al. 2011). Despite substantial methodological advances, reliable change detection remains challenging because genuine surface changes are often mixed with non-semantic variations caused by atmospheric conditions, sensor noise, seasonal illumination differences, and imperfect image registration (Chen and Bruzzone 2022; Cheng et al. 2024; Fang et al. 2022). Early unsupervised CD approaches primarily relied on algebraic transformations of bi-temporal observations, including image differencing, ratio-based operators, change vector analysis (CVA), fuzzy logic, and Fourier transformation (Bruzzone and Bovolo 2012; Bruzzone and Prieto 2000; Fang et al. 2022; Firouzabadi and Ramachandran 2000; Safa et al. 2023). These approaches

are computationally simple and remain important baselines, but their pixel-wise decision mechanisms generally do not explicitly model spatial dependencies between neighboring pixels. Consequently, isolated false alarms and fragmented change regions may appear in areas affected by radiometric variability or registration errors (Bruzzone and Bovolo 2012; Fang et al. 2022). Statistical and machine-learning approaches, including principal-component-based methods, clustering, support-vector machines, and random forests, subsequently introduced more sophisticated representations of the difference information (Bovolo et al. 2008; Celik 2009; Nielsen et al. 1998; Zhu et al. 2017). Although these approaches can improve discrimination between changed and unchanged classes, many still require empirical parameter selection, statistical assumptions, or auxiliary training information. The incorporation of spatial context led to the development of probabilistic graphical models, particularly Markov Random Fields (MRFs), for unsupervised change detection. MRFs provide a principled framework for representing the spatial dependency between neighboring pixels and formulating change detection as a global energy-minimization problem rather than as a collection of independent pixel decisions. One of the early influential applications was presented by Bruzzone and Fernández-Prieto, who incorporated spatial-contextual information through an MRF formulation for automatic analysis of the difference image in unsupervised change detection (Bruzzone and Prieto 2000). Their work demonstrated that incorporating neighborhood information could improve the discrimination of changed and unchanged regions compared with purely pixel-independent analysis.

Subsequent studies further developed MRF-based change detection by modifying the representation of the difference information and the spatial model. Kasetkasem and Varshney formulated an image change detection algorithm based on MRF models, explicitly exploiting spatial dependencies in the change map (Kasetkasem and Varshney 2002). Shi et al. later combined a spatially constrained chi-squared transformation with an MRF model for unsupervised multispectral change detection, demonstrating the benefit of incorporating spatial constraints to suppress scattered false detections (Shi et al. 2016). He et al. introduced an adaptive super pixel-based MRF framework in which spatial relationships were modeled at the super pixel level through a region-adjacency graph, providing a more object-oriented spatial representation for unsupervised change detection (He et al. 2018). More recently, Fang et al. proposed an unsupervised framework combining weighted change vector analysis with an improved MRF for high-spatial-resolution imagery. Their approach improves the difference image before applying an MRF-based spatial refinement and demonstrates the continuing relevance of MRFs for unsupervised remote sensing change detection (Fang et al. 2022). Despite these developments, an important characteristic of existing MRF-based CD frameworks is that the quality of the resulting change map depends strongly on the formulation of the energy function and the strategy used to minimize it. MRF inference is inherently a discrete optimization problem, and different optimization strategies have therefore been investigated, including Iterated Conditional Modes (ICM), graph-based minimization, and stochastic approaches such as simulated annealing (Kirkpatrick et al. 1983). ICM is computationally simple but can become trapped in local minima, whereas graph-cut methods provide powerful optimization capabilities for particular classes of energy functions but require specific conditions on the underlying pairwise potentials. Simulated annealing provides a more general stochastic mechanism for exploring complex discrete energy landscapes and has consequently been considered among the optimization strategies for MRF-based change-detection models.

The development of quantum annealing has subsequently introduced another perspective on discrete energy minimization. Quantum annealing and related quantum-assisted optimization approaches are particularly relevant to problems that can be represented as Ising or Quadratic Unconstrained Binary Optimization (QUBO) models (Glover et al. 2022; Kadowaki and Nishimori 1998; McGeoch 2014). In this formulation, binary variables and pairwise interactions naturally provide a mathematical representation of many MRF energy functions. Consequently, an MRF formulated as a quadratic binary energy model can, in principle, be transferred to quantum-annealing hardware or evaluated using classical annealing emulators. A recent review by Misra et al. has highlighted the growing application of quantum annealing and QUBO formulations to remote-sensing processing problems, while also emphasizing that current applications remain constrained by hardware size, embedding requirements, and the need for appropriate classical and hybrid optimization strategies (Misra et al. 2026). The connection between MRFs and QUBO is particularly attractive for remote-sensing change detection because the binary changed unchanged labeling of image pixels is naturally compatible with quadratic binary optimization. However, simply rewriting an MRF energy function as a QUBO does not by itself resolve the practical challenges associated with heterogeneous satellite scenes. In particular, a spatial regularization coefficient that is fixed globally can impose the same degree of smoothness on regions with substantially different local radiometric and structural characteristics. A strong global regularizer can suppress isolated noise but may simultaneously remove narrow or fragmented genuine changes, whereas a weak regularizer may preserve fine structures at the expense of increased false alarms. Existing MRF-based CD studies have addressed spatial representation through modified difference measures, super pixels, region-adjacency structures,

or improved pairwise potentials (Fang et al. 2022; He et al. 2018; Shi et al. 2016) but the problem of determining an appropriate spatial regularization strength directly from localized scene context remains an important issue.

Another limitation concerns the representation of spatial neighborhoods. Conventional lattice-based MRF formulations frequently employ four-connected neighborhoods, while extensions to eight-connected structures can provide additional diagonal spatial relationships. However, treating orthogonal and diagonal neighbors identically ignores their different Euclidean distances on the image lattice. From a geometric perspective, horizontal and vertical neighbors are separated by one $\sqrt{2}$ lattice unit, whereas diagonal neighbors are separated by units. Therefore, an isotropic eight-neighbor formulation does not explicitly preserve this geometric distinction. Introducing a distance-aware weighting of the pairwise interactions provide a direct mechanism for incorporating the physical geometry of the discrete image lattice into the optimization model. Motivated by these observations, this study develops an unsupervised, training-free change-detection framework that combines context-aware spatial regularization with a QUBO representation of a patch-decomposed MRF energy model. The principal contribution is not merely the conversion of an existing MRF into QUBO, since MRFs, QUBO formulations, and annealing-based optimization are individually established concepts (Glover et al. 2022; Kadowaki and Nishimori 1998; Kasetkasem and Varshney 2002; McGeoch 2014; Misra et al. 2026).

Instead, the contribution lies in their integration with two specifically designed spatial mechanisms:

a context-aware formulation that determines the spatial smoothness strength from localized statistics of the change-intensity field, and an anisotropic weighted eight-connected neighborhood in which diagonal interactions are reduced according to their greater lattice distance. This formulation is designed to address the competing requirements of false-alarm suppression and preservation of fine structural boundaries without relying on supervised training or a globally optimized spatial regularization coefficient. The resulting framework is evaluated on the Onera Satellite Change Detection (OSCD) benchmark, (Daudt et al. 2018) to examine whether localized context-aware regularization and distance-weighted spatial interactions provide measurable benefits over fixed isotropic MRF configurations and conventional unsupervised change-detection baselines (Chen and Bruzzone 2022). In addition to evaluating the final model, the study separately examines fixed-, context-aware four-neighbor, isotropic eight-neighbor, and distance-weighted eight-neighbor configurations. This controlled progression makes it possible to distinguish the contribution of context-aware regularization from that of the proposed spatial topology and to assess whether the combination of the two mechanisms provides a more balanced change-detection solution.

# 2. Methodology

## *2.1. framework*

The implementation is structured into three main phases:

Data Preparation and Decomposition: Bi-temporal multispectral bands are radiometrically calibrated using histogram matching. The scenes are partitioned into localized, overlapping tiles ($32 \times 32\, pixels$) using a spatial buffer to mitigate potential edge artifacts.

QUBO Construction: A binary quadratic model is defined for each tile, where individual pixels correspond to binary variables ($x_s \in \{0,1\}$) representing the unchanged and changed states. The linear biases are determined by a baseline threshold ($\lambda = 0.10$)evaluated against intensity differences. The quadratic couplings are governed by an adaptive beta parameter computed patch-by-patch from local standard deviations. To balance structural preservation with noise suppression, the pairwise grid is extended to an 8-connected graph where diagonal interactions are scaled by a distance decay factor of $\frac{1}{\sqrt{2}} \approx 0.707$. (Fang et al. 2022).

Reconstruction: The binary solution vectors from the optimization arrays are reassembled using a coordinate mapping step to reconstruct the global bitemporal change map for quantitative validation.

The complete end-to-end architecture of this three-phase framework is visually summarized in Fig. 1.

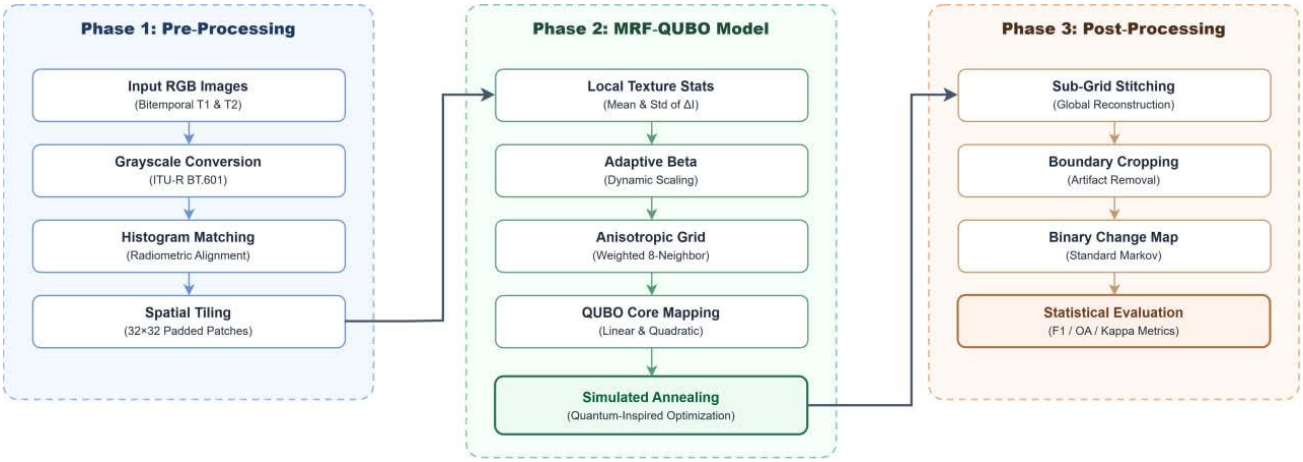



**Fig. 1** Schematic workflow of the proposed unsupervised change detection framework, spanning from raw data ingestion to core MRF-QUBO optimization and binary map reconstruction.

## *2.2. Spatial Patch Decomposition and Data Preparation*

To handle structural density and hardware graph embedding constraints, the bi-temporal remote sensing scenes are processed using a localized tile-based decomposition rather than global graph computation. The original data ingestion pipeline yields bi-temporal multi-channel structures $X_{T1}, X_{T2} \in \mathbb{R}^{H \times W \times 3}$ containing the standard red, green, and blue (RGB) spectral bands. Here, $H$ represents the continuous image brightness value and $W$ represents the image width in pixels. To fulfill the single-band structural constraints of our discrete optimization engine, a radiometric luminance reduction is executed directly on the multi-channel matrices. The transformation maps the three-dimensional color coordinates into a single-band grayscale spatial domain $\tilde{X}_{T1}, \tilde{X}_{T2} \in \mathbb{R}^{H \times W}$ via a calibrated linear combination matching the ITU-R BT.601 standard weights (ITU-R BT.601-7 2011):

$$\tilde{X}(s) = 0.299 \cdot R(s) + 0.587 \cdot G(s) + 0.114 \cdot B(s) \tag{1}$$

where $s$ denotes a localized pixel coordinate site across the continuous scene geometry, while $R(s)$, $G(s)$, and $B(s)$ represent the discrete intensity values of the red, green, and blue spectral channels at that specific pixel site, respectively.

Following the single-band transformation, a histogram matching calibration is applied to $\tilde{X}_{T2}$ using $\tilde{X}_{T1}$ as the baseline reference profile to neutralize ambient radiometric variations and illumination fluctuations across distinct temporal windows (Chen and Bruzzone 2022). To resolve dimension mismatches with the fixed hardware patch sampler, the original shapes are dynamically padded. The grid pad dimensions $(P_h, P_w)$ are calculated as:

$$P_h = \Big(N - \big(H \pmod N\big)\Big) \pmod N \tag{2}$$

$$P_w = \Big(N - \big(W \pmod N\big)\Big) \pmod N \tag{3}$$

where $N = 32$ represents the fixed patch tile edge dimension, $P_h$ is the calculated padding height added to the rows, $P_w$ is the calculated padding width added to the columns, and $(\text{mod})$ denotes the modulo operation. The input single-band scenes are padded using a symmetric edge reflection mode to generate the structured lattices $X_{T1}^{\text{pad}}, X_{T2}^{\text{pad}} \in \mathbb{R}^{(H+P_h)\times(W+P_w)}$.

The padded configuration is partitioned into non-overlapping spatial patches $P_{i,j}$ evaluated across a localized grid coordinate system. The input pixel intensities are explicitly normalized to a [0, 1] scale. For each single-band patch, a normalized radiometric difference intensity profile $\Delta I \in \mathbb{R}^{N \times N}$ is evaluated via absolute pixel-wise subtraction:

$$\Delta I_s = \left| X_{T2}^{\text{pad}}(s) - X_{T1}^{\text{pad}}(s) \right| \tag{4}$$

where $\Delta I_s$ is the computed absolute radiometric change magnitude at pixel site $s$ within the discrete grid system $S = \{1,2,\dots,N \times N\}$, while $X_{T1}^{\text{pad}}(s)$ and $X_{T2}^{\text{pad}}(s)$ represent the intensity values (ranging from 0 to 255 for 8-bit radiometric resolution) of the padded images at time 1 and time 2, respectively (Misra et al. 2026).

## *2.3. Unsupervised Markov Random Field Energy Formulation*

Within each localized patch lattice, the unsupervised binary change detection problem is cast as a MAP estimation over a discrete MRF (Misra et al. 2026). Let $x = \{x_s\}_{s \in S}$ be the binary configuration of the scene, where $x_s \in \{0,1\}$ represents the state of pixel site $s$, with $x_s = 0$ denoting an unchanged pixel and $x_s = 1$ denoting a changed pixel (Besag 1986). According to the Hammersley-Clifford theorem, the total configuration probability follows a Gibbs distribution, allowing the MAP inference to be equivalent to minimizing a global energy function $E(x)$ (Besag 1986):

$$E(x) = E_{\text{data}}(x) + E_{\text{spatial}}(x) \tag{5}$$

where $E(x)$ represents the total potential energy of the configuration, $E_{\text{data}}(x)$ is the data fidelity term, and $E_{\text{spatial}}(x)$ is the spatial contextual dependency term.

The data fidelity term $E_{\text{data}}(x)$ evaluates point-wise radiometric shifts relative to an autonomous activation barrier $\lambda$, without requiring external pre-clustering or empirical model training. It is formulated linearly as:

$$E_{\text{data}}(x) = \sum_{s \in S} (\lambda - \Delta I_s)\, x_s \tag{6}$$

where $\lambda = 0.10$ acts as a fixed, spatially invariant baseline activation threshold across the single-band dataset, $\Delta I_s$ is the radiometric difference magnitude at site $s$, and $x_s$ is the binary label variable of that pixel. When $\Delta I_s > \lambda$, the linear weight coefficient becomes negative, favoring the selection of the changed state $(x_s = 1)$ to lower the energy (Misra et al. 2026).

## *2.4. Context-Aware Adaptive-Beta Formulation*

To adapt to the spatial heterogeneity of remote sensing scenes without empirical global tuning, we implement an autonomous context -aware parameterization for each patch lattice. For a localized single-band difference profile $\Delta I$, we evaluate the patch-level mean radiometric change magnitude $\mu_{\text{patch}}$ and its corresponding localized standard deviation $\sigma_{\text{patch}}$ as:

$$\mu_{\text{patch}} = \frac{1}{N \times N} \sum_{s \in S} \Delta I_s \tag{7}$$

$$\sigma_{\text{patch}} = \sqrt{\frac{1}{N \times N} \sum_{s \in S} \left(\Delta I_s - \mu_{\text{patch}}\right)^2} \tag{8}$$

where $\mu_{\text{patch}}$ represents the average change intensity across the $N \times N$ spatial tile, $\sigma_{\text{patch}}$ is the localized standard deviation measuring texture variance, and $s$ indexes the individual pixel sites within the patch grid system S.

The adaptive spatial smoothness weight coefficient, $\beta_{\text{adaptive}}$, is dynamically governed by a combined mapping function that scales the variance against the baseline distance to the activation barrier $\lambda$:

$$\beta_{\text{adaptive}} = \sigma_{\text{patch}} \cdot \left(1.0 - \left|\mu_{\text{patch}} - \lambda\right|\right) \tag{9}$$

where $\beta_{\text{adaptive}}$ is the calculated dynamic spatial smoothing factor. To ensure numerical stability and prevent the complete collapse of spatial interaction terms in highly homogeneous uniform scenes, an absolute floor clipping boundary is enforced:

$$\beta_{\text{adaptive}} = \max\left(0.001, \beta_{\text{adaptive}}\right) \tag{10}$$

where the $\max\left(0.001, \beta_{\text{adaptive}}\right)$ function guarantees that the dynamic smoothness factor never drops below a minimum baseline penalty of $0.001$, maintaining spatial coupling in uniform areas.

## *2.5. Weighted Hybrid 8-Connected Neighborhood Topology*

To improve edge preservation and structural fidelity under complex multi-temporal noise profiles, the pairwise MRF interaction grid is extended from a standard 4-connected structure into a Weighted Hybrid 8-Connected Neighborhood Topology (Fang et al. 2022). Let $N(s)$denote the structural neighborhood set around pixel site$s$. This system differentiates spatial interactions based on physical Euclidean distance paths, partitioning forward directed links into direct neighbors ($D_{\text{direct}}$)and diagonal neighbors $\left(D_{\text{diagonal}}\right)$:

$$D_{\text{direct}} = \{(0,1),(1,0)\} \tag{11}$$

$$D_{\text{diagonal}} = \{(1,1),(1,-1)\} \tag{12}$$

where $D_{\text{direct}}$ defines the horizontal and vertical neighboring offsets at a physical unit distance of 1, and $D_{\text{diagonal}}$defines the diagonal neighboring offsets at a physical distance of $\sqrt{2}$.

Only forward-directed neighbor offsets are used to ensure that each undirected pairwise interaction is counted exactly once. The corresponding neighboring index sets for a pixel site $s$ are defined as follows, where $d$ represents the spatial offset vector:

$$\mathcal{N}_s^{\text{direct}} = \{s + d : d \in \mathcal{D}_{\text{direct}}\} \tag{13}$$

$$\mathcal{N}_s^{\text{diagonal}} = \left\{s + d : d \in \mathcal{D}_{\text{diagonal}}\right\} \tag{14}$$

The localized spatial energy contribution $E_{\text{spatial}}(x)$penalizes configurations where adjacent sites exhibit divergent binary labels (Besag 1986). The energy weight is scaled geometrically, applying a distance decay factor of $0.7071$to diagonal links to account for their lower spatial correlation. The spatial coupling parameters are defined as:

$$E_{\text{spatial}}(\boldsymbol{x}) = \sum_{s \in S} \left( \sum_{r \in \mathcal{N}_s^{\text{direct}}} \beta_{\text{adaptive}} \cdot I(x_s \neq x_r) + \sum_{r \in \mathcal{N}_s^{\text{diagonal}}} 0.7071\, \beta_{\text{adaptive}} \cdot I(x_s \neq x_r) \right) \tag{15}$$

where $r$indexes the neighboring pixel sites belonging to the respective directional sets, and $I(x_s \neq x_r)$ represents the indicator function, which outputs 1 if the condition $(x_s \neq x_r)$is true and 0 otherwise.

The total configuration energy is minimized through the following QUBO objective function (Glover et al. 2022):

$$E_{\text{QUBO}}(\boldsymbol{x}) = \sum_s \boldsymbol{Q}_{ss}\, x_s + \sum_{s<r} \boldsymbol{Q}_{sr}\, x_s x_r \tag{16}$$

By rewriting the conditional pairwise terms via the identity $I(x_s \neq x_r) = x_s + x_r - 2x_s x_r$, the total unsupervised MRF configuration landscape is mapped into an equivalent QUBO mathematical structure (Kadowaki and Nishimori 1998). For each independent single-band patch, the upper-triangular QUBO coefficient matrix is explicitly instantiated by updating the diagonal linear biases $\boldsymbol{Q}_{(s,s)}$ and off-diagonal quadratic couplings $Q_{(s,r)}$:

$$\boldsymbol{Q}_{(s,s)} = \lambda - \Delta I_s + \sum_{r \in D_{\text{direct}}(s)} \beta_{\text{adaptive}} + \sum_{r \in D_{\text{diagonal}}(s)} 0.7071\, \beta_{\text{adaptive}} \tag{17}$$

$$\boldsymbol{Q}_{(s,r)} = \begin{cases} -2.0 \cdot \beta_{\text{adaptive}}, & \text{if } r \in D_{\text{direct}}(s) \\ -1.4142 \cdot \beta_{\text{adaptive}}, & \text{if } r \in D_{\text{diagonal}}(s) \end{cases} \tag{18}$$

where $Q_{(s,s)}$ denotes the linear cost coefficient (diagonal bias) for node $s$, and $\boldsymbol{Q}_{(s,r)}$represents the quadratic coupling coefficient between connected nodes $s$ and $r$ within the upper-triangular matrix setup. The value $-1.4142$ is the direct evaluation of the combined diagonal distance penalty $-2.0 \times 0.7071$ specified in the hybrid neighborhood configuration. This discrete spin-glass formulation is subsequently evaluated via simulated and physical annealing pipelines to retrieve the stable minimum-energy state without supervised parameter dependencies (Misra et al. 2026).

### *2.6. Spatial Reconstruction and Mapping*

Following the discrete optimization phase executed by the annealing samplers, the retrieved binary solution vectors are mapped back to spatial coordinates. Because the patching routine utilizes a strictly structured, non-overlapping grid layout, the output arrays are directly reassembled sequentially via localized block index placement:

$$X_{\text{padded}}[i_b : i_b + N, j_b : j_b + N] = \text{reshape}(\mathbf{x}^*, N, N) \tag{19}$$

where $X_{\text{padded}}$ represents the global padded binary image matrix, $i_b$ and $j_b$ denote the current row and column block coordinates varying by steps of $N = 32$, and $\mathbf{x}^* \in \{0,1\}^{N^2}$ is the optimized binary solution vector returned by the sampler and $\text{reshape}(\cdot)$ rearranges this 1D vector into a 2D $N \times N$ matrix format.

The final global binary change map is extracted by slicing the padded boundaries to match the original layout dimensions:

$$X = \text{X}_{\text{padded}}[: H, : W] \tag{20}$$

where $X \in \mathbb{R}^{H \times W}$ is the verified global change map output containing the original dimensions, used directly for point-to-point comparison against the ground truth arrays during quantitative validation.

### *2.6. Experimental Pipeline and Computational Environment*

To evaluate the quantitative capability of the adaptive framework, the structural workflow is deployed within a cloud-based Python environments utilizing a virtualized Google Colab workspace infrastructure. The execution pipeline interfaces directly with the D-Wave Ocean Software Development Kit (SDK) to formulate and map the upper-triangular QUBO coefficient matrices (Glover et al. 2022; Misra et al. 2026). Instead of executing initial validation trials directly on physical quantum annealing hardware layouts, the discrete configuration energy landscapes are resolved locally using a high-fidelity classical emulation network (Misra et al. 2026). Specifically, the optimization arrays are processed using the Simulated Annealing Sampler architecture from the native D-Wave neal library backend, executing a configured sampling density of exactly $R = 35$ independent reads per single-band spatial tile to ensure stable ground-state convergence. The computational architecture evaluates the unsupervised optimization models across the bi-temporal image pairs (before and after) of the benchmark OSCD dataset (Chen and Bruzzone 2022). The dataset profiles bi-temporal, high-resolution imagery capturing complex urban expansions, agricultural shifts, and land-cover transitions across diverse global topographies, focusing on a multi-site validation tracking matrix comprising the targets of Abu Dhabi, Aguas Claras, Beihai, Bercy, Bordeaux, Hong Kong, Mumbai, Nantes, and Rennes (Chen and Bruzzone 2022).

## 3. Result

### *3.1. Hyperparameter Sensitivity Analysis (Fixed Isotropic Beta)*

To systematically evaluate the sensitivity of the spatial regularization parameter, a comprehensive grid-search experiment was conducted across the multi-temporal remote sensing database. During this analysis, the local intensity difference threshold ($\lambda$)was held strictly constant at a baseline value of $0.10$, while the isotropic smoothness weight ($\beta$)was manually varied across eleven discrete increments ranging from $0.00$ to $0.40$. The ensemble average of the quantitative evaluation metrics computed across all target satellite scenes is reported in Table 1. As demonstrated by the empirical values in Table 1, the regularization parameter $\beta$exerts a profound, coupled trade-off between the precision and recall capabilities of the MRF-QUBO pipeline. When $\beta = 0.00$, the pairwise spatial interaction energy terms are fully deactivated, reducing the framework to a localized pixel-level change detector. Under this independent state, the framework achieves its maximum recorded Average Recall of $0.4806$, yet it suffers from an unacceptably low Average Precision of $0.1971$. This severe statistical imbalance is directly attributed to the presence of pervasive salt-and-pepper noise and localized registration errors that remain unsuppressed due to the complete lack of spatial-contextual filtering. Conversely, incrementally scaling the smoothness penalty $\beta$ from $0.01$ to $0.05$ introduces Markovian contextual constraints that penalize isolated, high-frequency label transitions. This cooperative interaction effectively filters stochastic noise and drives the Average Precision up continuously, growing from $0.2458$ at $\beta = 0.01$ to $0.3540$ at $\beta = 0.05$. As $\beta$ increases further toward $0.40$, the precision continues to rise, reaching its maximum value of $0.5353$.

However, this precision gain comes at the direct cost of severe boundary erosion. As $\beta$scales upward, the excessive quadratic smoothing penalty overrides the unary data-fidelity term within the QUBO energy functional. Consequently, the optimizer enforces uniform regional smoothness, which aggressively wipes out authentic, fine-

grained structural changes, causing the Average Recall to drop continuously from $0.4606$ at $\beta = 0.01$ down to a minimum of $0.2178$ at $\beta = 0.40$. The aggregate F1-score manifests a classic parabolic sensitivity trajectory with respect to the isotropic smoothness weight. The optimization equilibrium is achieved at the empirical peak of $\beta = 0.05$, yielding the bestbalanced baseline F1-score of 0.3488 and a Cohen's Kappa of 0.3309. Beyond $\beta = 0.05$, the rapid decline in recall outweighs the precision gains, forcing the F1-score to decay significantly down to $0.2428$ at $\beta = 0.40$. This high sensitivity underscores the difficulty of tuning global, uniform hyperparameters in heterogeneous satellite imagery scenes and establishes the empirical necessity for an adaptive approach.

**Table 1** Quantitative evaluation of hyperparameter sensitivity analysis regarding the fixed isotropic smoothing factor ($\boldsymbol{\beta}$)under a constant threshold ($\boldsymbol{\lambda = 0.10}$) across the multi-temporal remote sensing database

| $\boldsymbol{\beta}$ | Avg. Precision | Avg. Recall | Avg. OA | Avg. F1-Score | Avg. Cohen's Kappa |
|---|---|---|---|---|---|
| 0.00 | 0.1971 | 0.4806 | 0.9297 | 0.2690 | 0.2442 |
| 0.01 | 0.2458 | 0.4606 | 0.9413 | 0.3033 | 0.2811 |
| 0.02 | 0.2808 | 0.4455 | 0.9475 | 0.3228 | 0.3021 |
| 0.03 | 0.3087 | 0.4307 | 0.9517 | 0.3349 | 0.3154 |
| 0.04 | 0.3364 | 0.4233 | 0.9547 | 0.3471 | 0.3286 |
| 0.05 | 0.3540 | 0.4095 | 0.9565 | 0.3488 | 0.3309 |
| 0.10 | 0.4336 | 0.3584 | 0.9621 | 0.3481 | 0.3324 |
| 0.15 | 0.4730 | 0.3205 | 0.9648 | 0.3309 | 0.3163 |
| 0.20 | 0.4963 | 0.2959 | 0.9655 | 0.3167 | 0.3028 |
| 0.30 | 0.5154 | 0.2478 | 0.9660 | 0.2713 | 0.2580 |
| 0.40 | 0.5353 | 0.2178 | 0.9664 | 0.2428 | 0.2300 |

## *3.2. Localized Scene Analysis at the Optimal Isotropic Baseline*

To evaluate the spatial filtering performance across distinct geographic and architectural landscapes, a scene-by-scene analysis was conducted under the optimal fixed baseline configuration ($\beta = 0.05$, $\lambda = 0.10$). Under this non-adaptive regime, the spatial regularization penalty is applied uniformly across all imagery sub-graphs, ignoring localized structural variations. The performance metrics computed for each of the nine scenes in the OSCD dataset are reported in Table 2. As demonstrated in Table 2, the uniform application of $\beta = 0.05$ results in highly volatile performance trajectories across different urban layouts. In regions with macro-scale, continuous changes like *Rennes*, the framework achieves its highest localized performance with an F1-score of $0.6177$ and a recall of $0.7354$. Similarly, in structured urban environments like *Nantes*, the spatial context successfully suppresses registration errors and noise, yielding a precision of $0.6354$and an F1-score of $0.4758$. However, because this global threshold cannot adapt to local patch statistics, it causes severe boundary erosion in intricate or fragmented landscapes. This rigid regularizer heavily penalizes authentic high-frequency transitions, leading to suppressed recall rates in structured environments like *Bercy* $(0.2847)$and *Aguas Claras* $(0.2319)$. Most notably, in complex, low-contrast scenes like *Bordeaux*, the fixed regularization fails drastically, collapsing to an F1-score of $0.0704$. This extreme regional volatility underscores the primary limitation of global MRF-QUBO configurations and justifies the need for context-aware adaptive models.

**Table 2** Detailed scene-by-scene change detection performance metrics under the optimal fixed isotropic baseline configuration ($\boldsymbol{\beta = 0.05, \lambda = 0.10}$)across the OSCD dataset

| City | Precision | Recall | OA | F1-Score | Kappa |
|---|---|---|---|---|---|
| Abu Dhabi | 0.2687 | 0.4912 | 0.9284 | 0.3464 | 0.3094 |
| Aguas Claras | 0.1687 | 0.2319 | 0.9641 | 0.1952 | 0.1755 |
| Beihai | 0.4926 | 0.4726 | 0.9743 | 0.4824 | 0.4691 |
| Bercy | 0.4356 | 0.2847 | 0.9921 | 0.3441 | 0.3402 |
| Bordeaux | 0.0476 | 0.1354 | 0.9572 | 0.0704 | 0.0549 |
| Hongkong | 0.1345 | 0.5126 | 0.8611 | 0.2125 | 0.1639 |
| Mumbai | 0.4682 | 0.3412 | 0.9734 | 0.3946 | 0.3799 |
| Nantes | 0.6354 | 0.3804 | 0.9907 | 0.4758 | 0.4711 |
| Rennes | 0.5328 | 0.7354 | 0.9743 | 0.6177 | 0.6045 |
| Average | 0.3538 | 0.3984 | 0.9573 | 0.3488 | 0.3409 |

### *3.3. Evaluation of the Autonomous 4-Neighbor Framework*

To overcome the limitations of manual parameter tuning, the proposed fully autonomous framework was evaluated using a traditional 4-connected neighborhood topology. In this scheme, the smoothness weight $\beta$ is calculated dynamically for each independent $32 \times 32$ image tile based on its localized statistical properties. The scene-by-scene performance metrics for this architecture are reported in Table 3. As shown in Table 3, transitioning to an automated adaptive-beta mechanism provides a more stable baseline across varying urban densities, yielding a solid Average F1-score of 0.3418. By adjusting the regularization weight according to local patch statistics, the model successfully avoids global over-smoothing. For instance, in dynamic scenes like *Rennes*, it maintains a high F1-score of 0.6019 and a strong recall of 0.7618. Similarly, complex environments like *Nantes* achieve an enhanced balance with a precision of 0.5505and an F1-score of 0.4589. However, the primary limitation of this setup lies in its restricted structural connectivity. The isotropic 4-connected topology fails to capture diagonal pixel dependencies, which leads to suboptimal edge preservation and boundary fragmentation in highly intricate or fragmented scenes such as Bordeaux (0.0774 F1-score). This geometric restriction demonstrates that while statistical automation is effective, a higher-order weighted neighborhood is required to resolve complex geographic details.

**Table 3** Detailed scene-by-scene change detection performance metrics under the proposed autonomous adaptive-beta framework using a 4-neighbor topology

| City | Precision | Recall | OA | F1-Score | Kappa |
|---|---|---|---|---|---|
| Abu Dhabi | 0.2623 | 0.5329 | 0.9261 | 0.3516 | 0.3171 |
| Aguas Claras | 0.1662 | 0.2365 | 0.9636 | 0.1952 | 0.1771 |
| Beihai | 0.4768 | 0.4767 | 0.9740 | 0.4767 | 0.4634 |
| Bercy | 0.3207 | 0.3069 | 0.9901 | 0.3136 | 0.3087 |
| Bordeaux | 0.0484 | 0.1924 | 0.9542 | 0.0774 | 0.0624 |
| Hongkong | 0.1362 | 0.5911 | 0.8518 | 0.2214 | 0.1735 |
| Mumbai | 0.4295 | 0.3401 | 0.9715 | 0.3796 | 0.3652 |
| Nantes | 0.5505 | 0.3934 | 0.9895 | 0.4589 | 0.4537 |
| Rennes | 0.4975 | 0.7618 | 0.9740 | 0.6019 | 0.5890 |
| AVERAGE | 0.3209 | 0.4257 | 0.9550 | 0.3418 | 0.3234 |

### *3.4. Evaluation of the Isotropic 8-Neighbor Framework*

To incorporate broader spatial relationships without directional bias, the autonomous adaptive-beta framework was evaluated using an isotropic 8-connected neighborhood topology, where all eight surrounding pixels share an identical interaction weight. The scene-by-scene performance metrics obtained under this configuration are presented in Table 4. As reported in Table 4, expanding the spatial context to an isotropic 8-neighbor scheme improves the classification baseline, achieving an Average F1-score of 0.3448 and a Cohen's Kappa of 0.3294. Incorporating

diagonal interactions without physical distance constraints enhances global metrics across dense scenes. For instance, structured environments like *Bercy* and *Nantes* deliver high precision values of 0.6360 and 0.7029, while dynamic landscapes like *Rennes* retain a solid F1-score of 0.5835. However, because this topology assigns identical weights to diagonal and orthogonal connections, it neglects the physical geometric distance $(\sqrt{2})$ . This lack of directional scaling introduces localized over-smoothing at sharp corners, leading to edge degradation and restricted recall rates in highly complex target environments like *Bordeaux* (0.0405). This volatility establishes the clear necessity for an anisotropic distance-decay modification to resolve precise structural borders.

**Table 4** Detailed scene-by-scene change detection performance metrics under the proposed autonomous adaptive-beta framework using an isotropic 8-neighbor topology

| City | Precision | Recall | OA | F1-Score | Kappa |
|---|---|---|---|---|---|
| Abu Dhabi | 0.3694 | 0.4781 | 0.9497 | 0.4168 | 0.3909 |
| Aguas Claras | 0.2973 | 0.2111 | 0.9760 | 0.2469 | 0.2350 |
| Beihai | 0.5404 | 0.3981 | 0.9766 | 0.4584 | 0.4468 |
| Bercy | 0.6360 | 0.2706 | 0.9935 | 0.3796 | 0.3769 |
| Bordeaux | 0.0267 | 0.0840 | 0.9603 | 0.0405 | 0.0258 |
| Hongkong | 0.1533 | 0.6109 | 0.8659 | 0.2451 | 0.1995 |
| Mumbai | 0.5729 | 0.2686 | 0.9761 | 0.3657 | 0.3552 |
| Nantes | 0.7029 | 0.2476 | 0.9903 | 0.3662 | 0.3624 |
| Rennes | 0.5737 | 0.5937 | 0.9781 | 0.5835 | 0.5723 |
| AVERAGE | 0.4303 | 0.3514 | 0.9629 | 0.3448 | 0.3294 |

## *3.5. Evaluation of the Proposed Weighted Hybrid 8-Neighbor Framework*

The final evaluation covers the primary innovation of this study: the autonomous adaptive-beta framework integrated with an anisotropic, weighted hybrid 8-neighbor topology. In this setup, diagonal pixel couplings are scaled by a physical distance decay factor of 0.7071to preserve spatial-geometric consistency across the lattice. The scene-by-scene results are reported in Table 5. As shown in Table 3, 4, and 5, introducing the geometric weight decay allows the framework to achieve the highest optimization balance among all autonomous variants, maximizing the Average F1-score at 0.3483and Cohen's Kappa at 0.3323. By penalizing diagonal interactions based on real physical Euclidean distance, the framework mitigates the over-smoothing drawback observed in isotropic systems. This geometric scaling significantly enhances structural recovery in dense environments; for example, *Nantes* experiences a notable rise in its localized F1-score to 0.4048. Simultaneously, the architecture maintains high regional stability in highly dynamic landscapes, as demonstrated by the strong F1-score of 0.6052 in *Rennes*. These improvements confirm that embedding anisotropic physical grid relationships directly into the QUBO matrix layout enables the quantum annealing optimizer to preserve structural edge topologies while rigorously filtering radiometric false alarms.

**Table 5** Detailed scene-by-scene change detection performance metrics under the proposed fully autonomous adaptive-beta framework integrated with an anisotropic, weighted hybrid 8-connected neighborhood topology across the OSCD dataset

| City | Precision | Recall | OA | F1-Score | Kappa |
|---|---|---|---|---|---|
| Abu Dhabi | 0.3474 | 0.4964 | 0.9460 | 0.4088 | 0.3814 |
| Aguas Claras | 0.2516 | 0.2104 | 0.9736 | 0.2292 | 0.2158 |
| Beihai | 0.5235 | 0.4221 | 0.9761 | 0.4674 | 0.4553 |
| Bercy | 0.4967 | 0.2859 | 0.9926 | 0.3629 | 0.3594 |
| Bordeaux | 0.0307 | 0.1038 | 0.9583 | 0.0474 | 0.0324 |
| Bongkong | 0.1499 | 0.6086 | 0.8630 | 0.2405 | 0.1944 |
| Mumbai | 0.5411 | 0.2792 | 0.9755 | 0.3683 | 0.3571 |
| Nantes | 0.6614 | 0.2917 | 0.9903 | 0.4048 | 0.4007 |
| Rennes | 0.5755 | 0.6381 | 0.9785 | 0.6052 | 0.5942 |
| AVERAGE | 0.3975 | 0.3707 | 0.9615 | 0.3483 | 0.3323 |

Additionally, preliminary grid-search trials over the intensity difference threshold ($\lambda$) indicated that maintaining $\lambda = 0.10$provides the optimal trade-off for unary data-fidelity, as lower values scale up radiometric false alarms, while higher thresholds suppress true change structural components. The qualitative change detection results for three representative cities are visually presented in Fig. 2

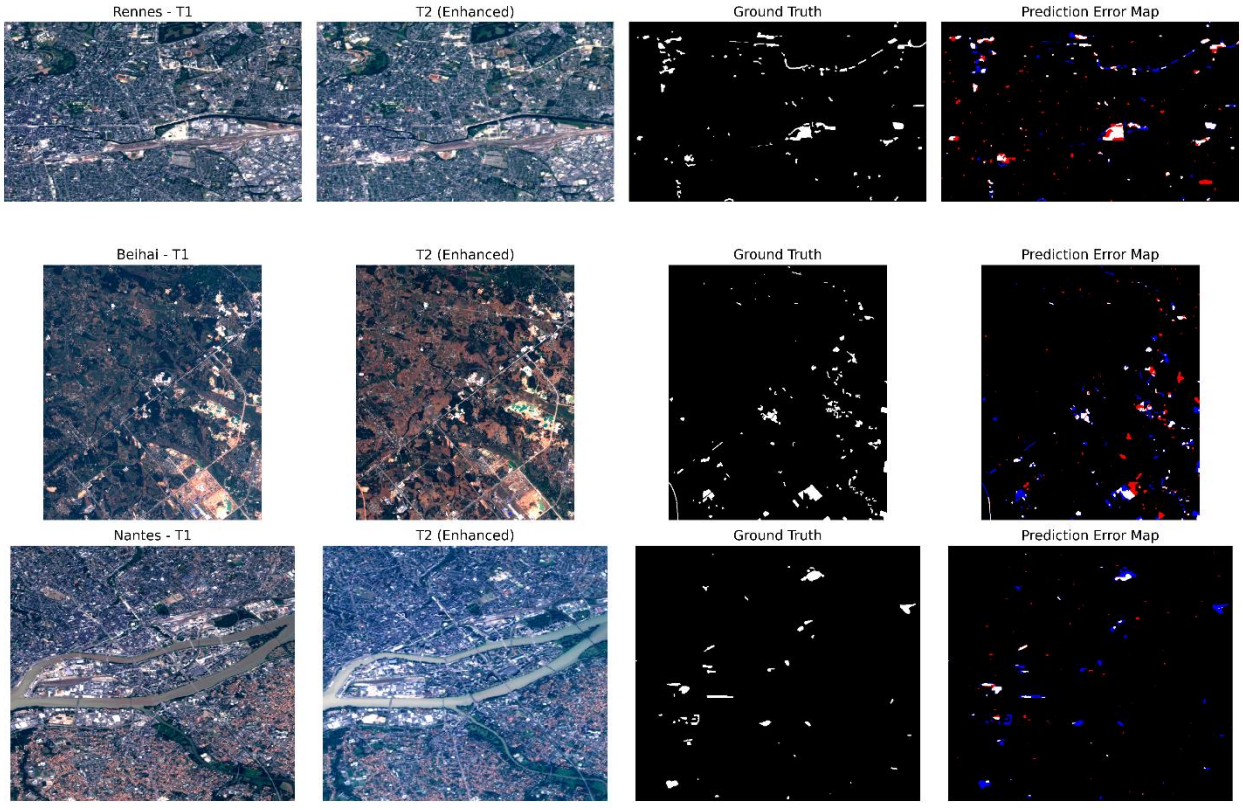



**Fig. 2** Qualitative visual comparison of the proposed change detection results for three representative OSCD cities. From left to right: reference image at Time 1, reference image at Time 2, ground truth, predicted change map, and the weighted hybrid error map. The Weighted Hybrid Error Map uses white for true positives (TP), red for false positives (FP), and blue for false negatives (FN)

# 4. Discussion

The results in Table 6 provide a useful comparison between the proposed weighted hybrid 8-neighbor MRF-QUBO framework and several conventional unsupervised thresholding methods evaluated under the same experimental setting.

**Table 6** Performance comparison of the proposed weighted hybrid 8-neighbor MRF-QUBO framework with conventional unsupervised change-detection methods on the OSCD dataset

| Method | Precision | Recall | OA | F1-Score | Kappa |
|---|---|---|---|---|---|
| Otsu | 0.1317 | 0.5915 | 0.8547 | 0.1987 | 0.1702 |
| Kapur | 0.4632 | 0.1453 | 0.9775 | 0.2026 | 0.1946 |
| Kittler-Illingworth | 0.1833 | 0.4928 | 0.9295 | 0.2510 | 0.2274 |
| Rosin | 0.2262 | 0.4140 | 0.9555 | 0.2866 | 0.2663 |
| IMG Diff (Bruzzone and Prieto 2000) | - | 0.6340 | - | - | - |
| GLRT (Bruzzone and Prieto 2000) | - | 0.6050 | - | - | - |
| Log ratio (Bruzzone and Prieto 2000) | - | 0.5970 | - | - | - |
| Proposed (8-N) | 0.3975 | 0.3707 | 0.9615 | 0.3483 | 0.3323 |

This proposed method achieves a precision of 0.3975, a recall of 0.3707, an overall accuracy (OA) of 0.9615, an F1-score of 0.3483, and a Kappa coefficient of 0.3323. Among the conventional thresholding methods, Rosin obtains the highest F1-score (0.2866), followed by Kittler–Illingworth (0.2510), Kapur (0.2026), and Otsu (0.1987). Thus, under the evaluation protocol used in this study, the proposed method provides the highest F1-score among the methods included in Table 6. The results also show that a higher OA does not necessarily correspond to better change-detection performance. For example, Kapur obtains an OA of 0.9775, which is higher than the 0.9615 obtained by the proposed method, but its F1-score is only 0.2026. This difference is important for the OSCD experiment because unchanged pixels constitute a large portion of the image. Consequently, OA alone can provide an incomplete picture of the ability to identify changed regions. The F1-score, together with precision and recall, provides a more informative description of the balance between correctly detected changes and false detections. And proposed method achieves a higher precision than Otsu, Kittler–Illingworth, and Rosin, while its recall is lower than those three methods. This indicates that the spatial regularization introduced by the MRF formulation does not simply increase the number of pixels classified as changed. Instead, it produces a more conservative change map in which some potential changes are rejected in favor of reducing false detections. The resulting F1-score of 0.3483 reflects the balance obtained between these two effects. In this respect, the context-aware β formulation plays an important role because the spatial smoothness penalty is determined from local patch characteristics rather than being fixed uniformly across the entire image. The comparison with the conventional thresholding methods also highlights the role of spatial information. Otsu, Kapur, Kittler–Illingworth, and Rosin determine the change threshold primarily from the statistical characteristics of the input distribution. Such approaches are computationally simple and do not require model training, but they do not explicitly represent relationships between neighboring pixels. The proposed framework retains the information provided by the image difference while introducing a spatial energy term through the MRF formulation. This allows neighboring pixels to influence the final binary decision and can help suppress isolated detections that are inconsistent with their local surroundings. The weighted hybrid 8-neighbor topology further extends this spatial formulation. In a conventional 4-connected graph, each pixel interacts only with its horizontal and vertical neighbors. The inclusion of diagonal interactions provides additional spatial relationships, while assigning a lower weight to diagonal terms according to their larger physical distance prevents them from being treated identically to the directly adjacent pixels. This formulation is intended to provide a more balanced representation of local spatial continuity, particularly around oblique or irregular structures. However, the present results do not establish that the 8-neighbor configuration is optimal for all types of remote-sensing imagery. A systematic comparison between different neighborhood structures would be required to isolate the contribution of the proposed topology.

The context-aware β formulation has a similar limitation. Its main motivation is to avoid using the same degree of spatial smoothing in regions with substantially different local characteristics. Highly textured or structurally complex regions often exhibit higher variance that could introduce dispersed radiometric false alarms, thus requiring stronger spatial regularization to suppress isolated noise. Conversely, homogeneous patches are inherently uniform and produce fewer spurious variations, allowing them to be processed with weaker smoothing. Using local patch

statistics provides a simple mechanism for introducing this spatial variability. Nevertheless, the effectiveness of this strategy depends on the reliability of the selected local statistic and on the patch size. Different patch sizes may produce different estimates of local context and consequently different spatial penalties. Therefore, the current formulation should not be interpreted as eliminating the general sensitivity of MRF-based methods to parameterization; rather, it changes the way the spatial parameter is determined. The Image Difference, GLRT, and Log-ratio methods are also included in Table 6 as additional reference methods. Their reported recall values are 0.6340, 0.6050, and 0.5970, respectively (Bruzzone and Prieto 2000). Since the other evaluation measures for these three methods are not reported in the comparison, these values are not directly compared with the F1-score, precision, OA, or Kappa coefficient of the proposed method. They instead provide an indication of the recall obtained by these conventional change-detection approaches under their reported evaluation setting. An important characteristic of the proposed framework is that it is training-free. Unlike supervised and self-supervised deep-learning approaches, the method does not require a training dataset, learned feature representation, or iterative model training. This reduces the dependence on labeled data and makes the optimization process more transparent because the final decision is obtained from an explicitly defined energy function. At the same time, this characteristic also represents a limitation. Without learned spectral and spatial representations, the method has less capacity to model complex semantic patterns than modern data-driven approaches. Therefore, the proposed framework should be viewed as a complementary alternative for situations in which a training-free and explicitly formulated optimization model is desirable, rather than as a replacement for learning-based change-detection systems.

Another important point concerns the QUBO formulation. Reformulating the MRF energy as a QUBO problem provides a mathematically convenient representation for annealing-based optimization and makes the proposed framework compatible with quantum-annealing hardware. However, the experiments presented in this study were performed using simulated annealing. Therefore, the current results demonstrate the behavior of the proposed energy formulation under a classical annealing solver and should not be interpreted as evidence of quantum speedup or quantum computational advantage. Evaluation on a physical quantum annealing processor would be necessary to investigate those aspects. The patch-based implementation also introduces a spatial limitation. Because the image is divided into independent patches, pixels located near the boundaries of two neighboring patches may not have access to the same spatial context as pixels located inside a patch. This can lead to discontinuities along patch borders, particularly when the detected structures cross multiple patches. The issue is related to the current decomposition strategy rather than to the MRF or QUBO formulation itself. Overlapping patches, boundary constraints, or larger-scale graph connections could potentially reduce this effect in future implementations. The computational cost should also be considered. Although the patch decomposition makes the optimization problem more manageable and provides a direct route to QUBO construction, the total computational burden increases with the number of patches and the complexity of the annealing process. The present study therefore does not establish real-time performance. In particular, the statement that the formulation is suitable for near-real-time satellite monitoring would require dedicated timing experiments and, for the quantum case, evaluation on appropriate hardware. Such experiments are beyond the scope of the current study.

Overall, the results suggest that the proposed weighted hybrid 8-neighbor MRF-QUBO framework provides a reasonable training-free alternative for unsupervised change detection on OSCD. Its main contribution is the integration of local context-dependent spatial regularization, distance-weighted neighborhood interactions, and QUBO-based energy minimization within a single framework. The experimental results show an improvement in F1-score over the conventional thresholding methods included in Table 6, while also demonstrating that the method does not achieve the highest recall among all compared approaches. This trade-off reflects the central behavior of the proposed spatial regularization: reducing isolated or inconsistent detections while retaining meaningful structural changes. Further evaluation on additional datasets, different patch sizes and neighborhood configurations, and physical quantum annealing hardware would be valuable for determining the generality and computational potential of the proposed formulation.

# 5. Conclusion

This study proposed an unsupervised and training-free change detection framework based on the reformulation of a patch-decomposed Markov Random Field (MRF) as a Quadratic Unconstrained Binary Optimization (QUBO) problem. A context-aware β formulation was introduced to adjust the spatial smoothness according to local patch characteristics, together with a weighted hybrid 8-connected neighborhood to improve the balance between noise suppression and boundary preservation. Experiments on the OSCD dataset resulted in an Average F1-score of 0.3483 and an Overall Accuracy of 96.15%. The proposed framework does not require labeled data, external training, or

learned model parameters, while retaining a formulation that can be directly mapped to quantum annealing hardware. These results indicate the potential of combining contextual spatial modeling with QUBO-based optimization for training-free change detection. Future work will focus on overlapping patches and boundary-aware constraints to reduce discontinuities between independently processed image tiles and on evaluating the formulation using physical quantum annealing hardware

## Statements and Declarations

Funding: The authors declare that no funds, grants, or other support were received during the preparation of this manuscript.

Competing Interests: The authors have no relevant financial or non-financial interests to disclose.

## Author Contributions

Conceptualization: Saman Ghafari; Methodology: Saman Ghafari; Formal analysis: Saman Ghafari; Software: Shaho Piroti, Saman Ghafari; Data curation: Shaho Piroti; Writing - original draft preparation: Saman Ghafari; Writing - review and editing: Shaho Piroti, Parviz Zeaieanfirouzabadi.

**Data Availability Statement**

The datasets used in this study are publicly available from their respective sources, as cited in the manuscript. No new datasets were generated in this study. The data supporting the findings of this study are available from the corresponding author upon reasonable request.

The source code used in this study is available from the corresponding author upon reasonable request, and will soon be made publicly available on GitHub.

# 6. Reference

Besag J (1986) On the statistical analysis of dirty pictures. *J R Stat Soc Ser B Methodol* 48(3):259-279. https://doi.org/10.1111/j.2517-6161.1986.tb01412.x

Bovolo F, Bruzzone L, Marconcini M (2008) A novel approach to unsupervised change detection based on a semisupervised SVM and a similarity measure. *IEEE Trans Geosci Remote Sens* 46(7):2070-2082. https://doi.org/10.1109/TGRS.2008.916643

Brunner D, Bruzzone L, Lemoine G (2010) Change detection for earthquake damage assessment in built-up areas using very high resolution optical and SAR imagery. In: *Proc IEEE Int Geosci Remote Sens Symp (IGARSS)*, pp 3210-3213. https://doi.org/10.1109/IGARSS.2010.5651416

Bruzzone L, Bovolo F (2012) A novel framework for the design of change-detection systems for very-high-resolution remote sensing images. *Proc IEEE* 101(3):609-630. https://doi.org/10.1109/JPROC.2012.2197169

Bruzzone L, Prieto DF (2000) Automatic analysis of the difference image for unsupervised change detection. *IEEE Trans Geosci Remote Sens* 38(3):1171-1182. https://doi.org/10.1109/36.843009

Buch NE, Velastin SA, Orwell J (2011) A review of computer vision techniques for the analysis of urban traffic. *IEEE Trans Intell Transp Syst* 12(4):920-939. https://doi.org/10.1109/TITS.2011.2119372

Celik T (2009) Unsupervised change detection in satellite images using principal component analysis and k-means clustering. *IEEE Geosci Remote Sens Lett* 6(4):772-776. https://doi.org/10.1109/LGRS.2009.2025059

Chen Y, Bruzzone L (2022) Self-supervised change detection in multi-view remote sensing images. *IEEE Trans Geosci Remote Sens* 60:1-14. Art no. 4413911. https://doi.org/10.1109/TGRS.2021.3089453

Cheng G, Huang Y, Li X, Lyu S, Xu Z, Zhao H, Zhao Q, Xiang S (2024) Change detection methods for remote sensing in the last decade: a comprehensive review. *Remote Sens* 16(13):2355. https://doi.org/10.3390/rs16132355

Daudt RC, Le Saux B, Boulch A, Gousseau Y (2018) Urban change detection for multispectral earth observation using convolutional neural networks. In: *Proc IEEE Int Geosci Remote Sens Symp (IGARSS)*, pp 2115-2118. https://doi.org/10.1109/IGARSS.2018.8518015

Fang H, Du P, Wang X, Lin C, Tang P (2022) Unsupervised change detection based on weighted change vector analysis and improved Markov random field for high spatial resolution imagery. *IEEE Geosci Remote Sens Lett* 19:1-5. Art no. 2503105. https://doi.org/10.1109/LGRS.2021.3059461

Firouzabadi PZ, Ramachandran S (2000) Change information visualization using fuzzy logic. In: *Proc 22nd Urban Data Manag Symp*, Delft, Netherlands, GIS Technology II: Geomatics and Modelling, pp v77-v86.

Glover F, Kochenberger G, Hennig R, Du Y (2022) Quantum bridge analytics I: a tutorial on formulating and using QUBO models. *Ann Oper Res* 314(1):141-183. https://doi.org/10.1007/s10479-022-04634-2

He P, Shi W, Zhang H (2018) Adaptive superpixel based Markov random field model for unsupervised change detection using remotely sensed images. *Remote Sens Lett* 9(8):724-732. https://doi.org/10.1080/2150704X.2018.1470698

ITU-R (2011) Studio encoding parameters of digital television for standard 4:3 and wide-screen 16:9 aspect ratios. Recommendation ITU-R BT.601-7, International Telecommunication Union, Geneva, Switzerland.

Kadowaki T, Nishimori H (1998) Quantum annealing in the transverse Ising model. *Phys Rev E* 58(5):5355-5363. https://doi.org/10.1103/PhysRevE.58.5355

Kasetkasem T, Varshney PK (2002) An image change detection algorithm based on Markov random field models. *IEEE Trans Geosci Remote Sens* 40(8):1815-1823. https://doi.org/10.1109/TGRS.2002.802498

Kirkpatrick S, Gelatt CD, Vecchi MP (1983) Optimization by simulated annealing. *Science* 220(4598):671-680. https://doi.org/10.1126/science.220.4598.671

Liu Y, Pang C, Zhan Z, Zhang X, Yang X (2021) Building change detection for remote sensing images using a dual-task constrained deep Siamese convolutional network model. *IEEE Geosci Remote Sens Lett* 18:811-815. https://doi.org/10.1109/LGRS.2020.2988032

McGeoch CC (2014) *Adiabatic Quantum Computation and Quantum Annealing: Theory and Practice*. Morgan & Claypool Publishers, San Rafael. https://doi.org/10.2200/S00585ED1V01Y201407QMC008

Misra I, Moorthi SM, Dhar D (2026) Quantum annealing for remote sensing data processing: a review of optimization-based applications. *Remote Sens Appl Soc Environ* 41:101936. https://doi.org/10.1016/j.rsase.2026.101936

Nielsen AA, Conradsen K, Simpson JJ (1998) Multivariate alteration detection (MAD) and MAF postprocessing in multispectral, bitemporal image data. *Remote Sens Environ* 64(1):1-19. https://doi.org/10.1016/S0034-4257(97)00162-4

Safa R, Zeaieanfirouzabadi P, Tavakoli Sabour SM (2023) Satellite based band features change detection using discrete fractional Fourier transform. *Kharazmi J Earth Sci* 9(1):116-149. http://gnf.khu.ac.ir/article-1-2827-fa.html

Shi A, Wang C, Shen S, Huang F, Ma Z (2016) Unsupervised change detection of multispectral images based on spatial constraint chi-squared transform and Markov random field model. *J Appl Remote Sens* 10(4):046028. https://doi.org/10.1117/1.JRS.10.046028

581 Zhu XX, Tuia D, Mou L, Xia GS, Zhang L, Xu F, Fraundorfer F (2017) Deep learning in remote sensing: a
582 comprehensive review and list of resources. *IEEE Geosci Remote Sens Mag* 5(4):8-
583 36. https://doi.org/10.1109/MGRS.2017.2762307

584